



HAL
open science

The West African monsoon dynamics, Part II: The "pre-onset" and the "onset" of the summer monsoon

Benjamin Sultan, Serge Janicot

► **To cite this version:**

Benjamin Sultan, Serge Janicot. The West African monsoon dynamics, Part II: The "pre-onset" and the "onset" of the summer monsoon. *Journal of Climate*, 2003, 16, pp.3407-3427. 10.1175/1520-0442(2003)0162.0.CO;2 . hal-00155510

HAL Id: hal-00155510

<https://hal.science/hal-00155510>

Submitted on 28 Jan 2021

HAL is a multi-disciplinary open access archive for the deposit and dissemination of scientific research documents, whether they are published or not. The documents may come from teaching and research institutions in France or abroad, or from public or private research centers.

L'archive ouverte pluridisciplinaire **HAL**, est destinée au dépôt et à la diffusion de documents scientifiques de niveau recherche, publiés ou non, émanant des établissements d'enseignement et de recherche français ou étrangers, des laboratoires publics ou privés.

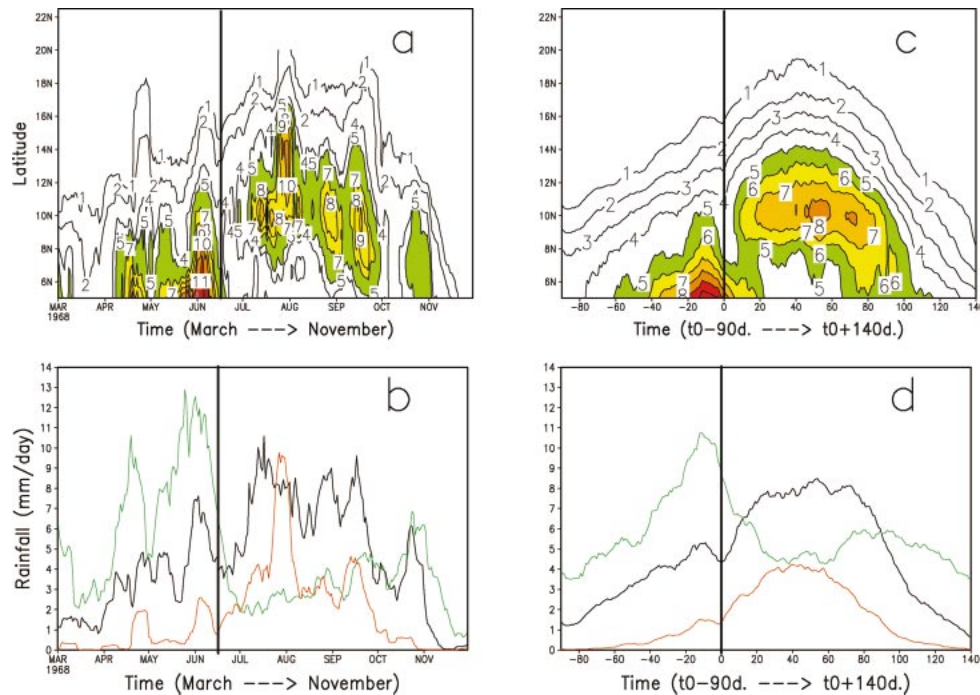


FIG. 4. (a) Time–lat diagram from 1 Mar to 30 Nov 1978 of daily rainfall (mm day^{-1}), averaged over 10°W – 10°E and filtered to remove variability lower than 10 days. Values greater than 5 mm day^{-1} are colored. (b) Time sections of diagram (a) at 5° (green curve), 10° (black curve), and 15°N (red curve). In (a) and (b), the vertical line localizes the date selected for the ITCZ shift (17 Jun). (c) Composite time–latitude diagram of daily rainfall (mm day^{-1}) averaged over 10°W – 10°E , filtered to remove rainfall variability lower than 10 days, and averaged over the period 1968–90 by using as the reference date the shift date of the ITCZ for each year. Values are presented from t_0 (the shift date) -90 days to $t_0 + 140$ days. Values greater than 5 mm day^{-1} are colored. (d) Time sections of diagram (c) at 5° (green curve), 10° (black curve), and 15°N (red curve). In (c) and (d), the vertical line localizes the date of the ITCZ shift at t_0 (the mean date over the period 1968–90 is 24 Jun).

rica, which is also evident in Fig. 4b by the crossing of the rainfall time series at 5° and 10°N .

As for the detection of the monsoon preonset, a quasi-objective method can be built up to define a date for the ITCZ latitudinal shift for each year between 1968 and 1990. An empirical orthogonal function (EOF) analysis (Richman 1986) has been performed on time–latitude diagrams of daily rainfall values averaged over 10°W – 10°E , for each year from 1 March to 30 November. Most of the rainfall variance decomposed by the EOF analysis is explained by the two first components. The first one (about 91% of the variance in 1968–90) is highly correlated with the rainfall time series at 10°N (correlation of 0.9 in 1968–90) and the second one (about 9% of the variance in 1968–90) is highly correlated with the rainfall time series at 5°N (correlation of 0.75 in 1968–90). The rainfall indexes (i.e., the rainfall time series) at 10° and at 5°N can then be used to sum up rainfall variability over West Africa and to define a date for the ITCZ shift. For few years, especially the dry ones like 1983 or 1984, we must have considered the rainfall index at 7.5° instead of 10°N because the axis of maximum rainfall is located at a more southern location in summer. The time series of the rainfall in-

dexes at 5° and 10°N for 1978 are shown in Fig. 4b. A rainfall maximum occurs during May–June when the ITCZ is located at 5°N . The abrupt shift of the ITCZ from 5° to 10°N can be defined by simultaneously, a decrease of the 5°N rainfall index and an increase of the positive slope of the 10°N rainfall index. Because of the lag between these two moments, an uncertainty of a few days remains. So we look for an increase of the positive slope of a similar rainfall index at 15°N during this time to specify an only date. For 1978 the date of 17 June has been selected (see vertical line in Fig. 4b).

This method has been used to define a date of the ITCZ shift for each year from 1968 to 1990. The mean date t_0 found for this shift over the period 1968–90 is 24 June and the standard deviation is 8.0 days. Correlations computed between the preonset dates and the onset dates ($r = 0.01$), as well as with the summer rainfall amount over the Sahel ($r = -0.16$ for the preonset dates, and $r = -0.21$ for the onset dates) are not significant over the period 1968–90, indicating that independent mechanisms control these different variables. To provide a more precise statistical distribution of these ITCZ shift dates, we have extended this analysis over

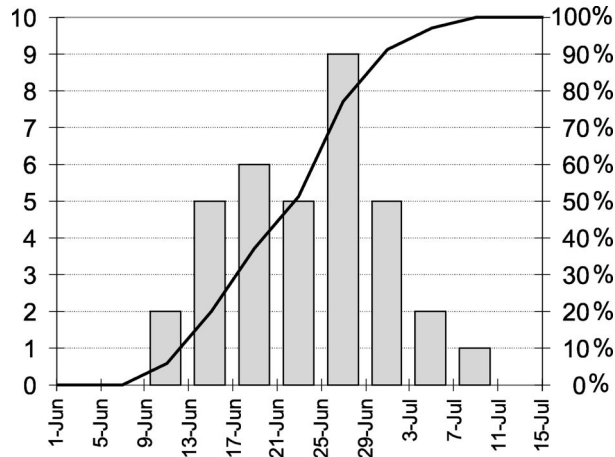


FIG. 5. Histogram of the ITCZ shift dates over the period 1968–2002 (bars; left scale) defined from the NOAA/OLR dataset, and the cumulative distribution function (line; right scale).

the period 1968–2002 by using the NOAA/OLR data. We first made sure that we can apply a similar approach to define these dates from OLR indexes at 5° and 10°N by verifying that we find dates similar or very close to those found with the IRD rainfall indexes during the common period 1979–90, then we defined the ITCZ shift dates from the OLR values over the period 1991–2002. Figure 5 shows the histogram of the ITCZ shift dates over the period 1968–2002 as well as the corresponding cumulative distribution function. Over this period, the averaged date is the same (24 June) and the standard deviation is very similar (7.0 days). This distribution can be used as the first step of a probabilistic forecast of the summer monsoon onset date over West Africa, based on a 35-yr dataset specific to a dry period compared to the long-term mean (Hastenrath 1995). Le Barbé et al. (2002) showed that the mean date of the ITCZ shift is not significantly different from the previous wet period 1950–70. So our probability distribution function may also be valuable for a different climate state, but as the approach of Le Barbé et al. is rather different from our approach, this point should be investigated more precisely; however, this is out of the scope of this paper. Hereafter, all the computations have been based on the period 1968–90 where the ITCZ shift dates have been defined from the IRD rainfall indexes, because we get a more precise signal from daily rainfall amounts measured at the station network than from twice-daily OLR measurements. We checked however that the conclusions inferred from the results presented below over the period 1968–90 are confirmed over the period 1968–2002.

Figure 4c shows the composite of the mean 10°W–10°E daily rainfall values averaged over the period 1968–90 by using the ITCZ shift date for each year as the respective reference date. This figure points out latitude–time rainfall variations between t_0 (the shift date) minus 90 days and t_0 plus 140 days. Figure 4d shows the cor-

responding rainfall indexes at 5°, 10°, and 15°N. The rainfall maximum at 5°N, also evident at 10° and 15°N, occurs about 10 days before t_0 . Then rainfall decreases slightly, but over West Africa it only decreases to a relative minimum value at the beginning of the ITCZ shift. At t_0 , the shift is detected by a new positive slope of the rainfall index at 10° and at 15°N. The ITCZ reaches the latitude 10°N about 10–20 days after t_0 where rainfall increases until mid-August. The withdrawal of the ITCZ is quite sharp too, except that the June rainfall maximum at 5°N has no counterpart in late summer when the monsoon retreats equatorward and we do not observe any rainfall minimum between the summer monsoon season and the second rainy season along the Guinea coast. This also offers a different view from the progression of the northern limit of the ITCZ (see the 1–4 mm day⁻¹ isolines), which has a more gradual latitudinal variation during the onset than during the withdrawal.

Figure 6 shows similar composite time–latitude diagrams but for OLR values and for meridional cross sections at particular longitudes, from 20°W to 10°E. Using OLR values enables us to test the previous results on an independent dataset and to consider a wider region without any spatial gap. At 0° (Fig. 6c) and at 10°W (Fig. 6b), the OLR patterns are very consistent with the rainfall (Fig. 4c). Again we see the shift of the ITCZ around t_0 , from the latitude 5°N at the time of the first rainy season over the Guinea coast region to the latitude 10°N at the time of the summer monsoon season over the Sudano–Sahelian region. This shift, as seen through the OLR values, is again concomitant with a temporary decrease of convection over all the latitudes of West Africa at this longitude. Similar results have been obtained at 5°E (not shown). At 10°E (Fig. 6d), the OLR pattern is a bit different. At this longitude as well as for more eastward longitudes crossing central Africa, the convection decrease at t_0 is still evident but the ITCZ shift does not occur anymore. The ITCZ progresses regularly to the north before t_0 and stays centered around 6°N after t_0 while its northern boundary extends northward during the first half of summer. Finally at 20°W over the ocean, the northward excursion of the ITCZ is even more regular with no latitudinal shift and no clear convection decrease at t_0 . These results suggest that the ITCZ shift leading to the abrupt summer monsoon onset is working well on the longitudes where a land–sea contrast exists between 10°W and 5°E, that is where the concept of the monsoon system, as a large-scale cross-equatorial atmospheric circulation from an oceanic basin on one side and a land area on the other side, is well established. Outside this longitudinal band, the ITCZ loses this particular behavior to show a rather progressive meridional excursion.

Although observed rainfall data are used in this work, the consistency of the seasonal cycle of precipitations in the NCEP–NCAR and ECMWF reanalyses has been examined to estimate the accuracy of the associated temporal fluctuations of the reanalysis winds (Sultan 2002;

atmospheric system. So in this section, to complement the results shown on rainfall and OLR (Figs. 4 and 6), we describe some of the main features of the monsoon seasonal cycle and its onset by using latitude cross sections averaged over the longitude band 10°W–10°E. Figure 7 depicts time–latitude diagrams for the relative vorticity at 925 hPa (Fig. 7a), the vertical velocity at 850 hPa (Fig. 7b), the vertical velocity averaged on 700–500 hPa (Fig. 7c), the meridional wind component at 600 hPa (Fig. 7d) and at 925 hPa (Fig. 7e), the zonal wind component at 600 hPa (Fig. 7f) and at 925 hPa (Fig. 7g), the vertical shear of the zonal wind between 925 and 600 hPa (Fig. 7h), the top of the monsoon layer (Fig. 7i), and the precipitable water height (Fig. 7j) (all of these diagrams are expressed in the referential $t_0 - 90/t_0 + 140$, where t_0 represents in average the 24 June for the monsoon onset).

The 925-hPa relative vorticity diagram (Fig. 7a) enables us to follow the meridional excursion of the ITF and of the heat low, expressed by positive maxima. From $t_0 - 90$ to $t_0 - 10$, the ITF moves gradually to the north, passing at 15°N around $t_0 - 40$, that is at the time of the monsoon preonset as we previously saw ($t_0 - 40$ is about the mean date defined for the preonset—14 May). From $t_0 - 10$, the northward movement of the ITF accelerates, passing at 17.5°N at t_0 and going northward until about $t_0 + 20$ when it reaches about 21°N and stays during most of the summer with its greatest values before retreating southward. South of 10°N, relative vorticity is negative with minima located between the equator and 3°N, which signs the anticyclonic curvature of the winds crossing the equator. Tomas and Webster (1997) showed that negative absolute vorticity during northern summer just north of the equator over the Guinea Gulf is a sign of inertial instability of the low-level atmospheric circulation. Both the highest negative values of relative and absolute vorticity occur at t_0 , suggesting that the summer monsoon onset is characterized by a maximum of inertial instability over the Guinea gulf, which is released when the monsoon begins to intensify.

Figure 7b depicts similar time–latitude diagram for the 850-hPa vertical velocity. It again enables us to follow the meridional excursion of the ITF and the associated heat low, represented by the axis of dry convection maximum in the low levels. Its seasonal migration is very similar, upward motion being associated with cyclonic vorticity. The greatest values are present around $t_0 - 80$, that is approximately at the beginning of April, then decrease regularly as the ITF moves to the north. However a temporary enhancement of dry convection occurs between $t_0 - 10$ and t_0 (it is the greatest at t_0) when the ITF is located at 17.5°N and when deep convection in the ITCZ, still located at 5°N, decreases (Figs. 4 and 6). Figure 7c (vertical velocity averaged on 700–500 hPa) and Fig. 7d (meridional wind component at 600 hPa) describe the upper part of the transverse circulation associated to the heat low. South

of the maximum of the upward 850-hPa vertical velocity, which is located at 17.5°N at t_0 , both the 600-hPa northerly wind and 700–500-hPa downward velocity have the greatest values around 12.5°N at t_0 , following a seasonal cycle similar to the one of 850-hPa vertical velocity. In the lower layers, the 925-hPa meridional wind (Fig. 7e) also has its greatest values at t_0 between 5° and 10°N. Then the whole meridional transverse circulation associated to the heat low has its greatest intensity at t_0 . Figure 7c shows that the subsiding branch of the low-level circulation, located at 12.5°N at t_0 , clearly separates the dry convection area in the north from the lower part of the deep convection associated to the ITCZ in the south.

The seasonal march of the ITF is also closely linked with the evolution of the African easterly jet (AEJ) described by the zonal wind component at 600 hPa, the pressure level of the jet core (Fig. 7f). This jet is located south of the ITF, between the dry convection area of the heat low and the deep convection of the ITCZ. The highest speed of the jet is observed close to t_0 at 10°N, concomitant with the enhancement of the low-level meridional circulation associated with the heat low and the northward acceleration of the relative vorticity maximum axis. This is consistent with the work of Thorncroft and Blackburn (1997) who showed that the AEJ is mostly controlled by the direct meridional circulation of the heat low, the northerly returning flow in the midlevels inducing an easterly acceleration due to the planetary vorticity advection. At 925 hPa (Fig. 7g), the westerly zonal wind is increasing in the latitude band 5°–15°N from about $t_0 - 30$, with a stronger acceleration at 10°N from $t_0 - 10$ (shown by the time section at this latitude), characterizing the monsoon enhancement. This leads to an increase of the vertical shear of the zonal wind between 925 and 600 hPa, which is the greatest at t_0 along 10°N (Fig. 7h).

This monsoon enhancement can be well characterized through the estimation of the top of the monsoon layer (Fig. 7i). This estimation has been defined following Lamb (1983) by the computation of the pressure levels where the zonal wind component equals zero, going from westerly downward to easterly upward. The areas shaded in Fig. 7i show the lowest pressure values, that is, the greatest depth of the monsoon layer. We must not consider the shaded areas in the upper corners, which correspond to the northern part of the anticyclonic cell controlling westerly winds at these latitudes and at these periods of the year. From $t_0 - 90$ to $t_0 - 10$, the top of the monsoon layer is located at a pressure level around 870 hPa and moves northward from 5° to 10°N. Then, the monsoon depth grows drastically and extends both northward and southward, during summer reaching 840 hPa north of 15°N and 760 hPa at 5°N. The monsoon onset is then characterized by an abrupt and large meridional and vertical development of the westerly wind layer as the ITCZ moves from 5° to 10°N. This evolution can be seen also in the precipitable water height for

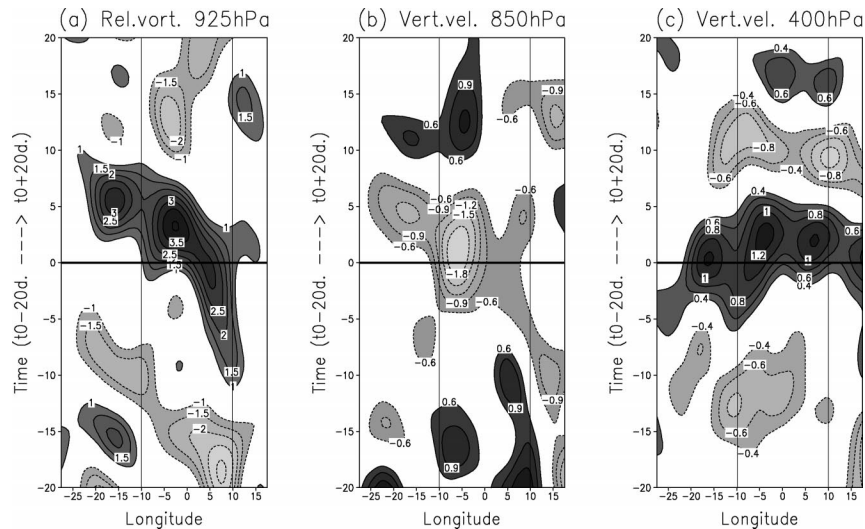


FIG. 10. Composite time-lon diagram of the 10–60-day filtered NCEP–NCAR 925-hPa relative vorticity (10^{-6} s^{-1}) at 17.5°N , averaged over the period 1968–90 by using the ITCZ shift date as the reference date for each year. Values are presented from t_0 (the shift date) minus 20 days to $t_0 + 20$ days. (b) Same as (a) but for the 850-hPa vertical velocity at 17.5°N (unit in 100 Pa s^{-1}). Negative values represent upward velocity. (c) Same as (b) but for 400-hPa vertical velocity at 10°N .

along the western coast of West Africa between 20° and 22.5°N . At $t_0 + 12$ and $t_0 + 15$, the westerly wind advection is maintained by a rather weak cyclonic circulation centered along 10°N while the northern cyclonic center is now visible over the ocean. The ITCZ get its final location at 10°N around $t_0 + 21$ with the appearance of rainfall minima along the Guinean coast. So the examination of the time series of the filtered wind field patterns enables to suggest that the summer monsoon onset is not only due to a meridional dynamics associated to the heat low but that it is also associated with a westward-propagating signal at an intraseasonal timescale, which induces the enhancement of the heat low rotational and transverse circulation.

Figure 10 helps to quantify these observations by depicting composite longitude–time diagrams of the 10–60-day filtered 925-hPa relative vorticity at 17.5°N (Fig. 10a), 850-hPa vertical velocity at 17.5°N (Fig. 10b), and 400-hPa vertical velocity at 10°N (Fig. 10c), computed between $t_0 - 20$ and $t_0 + 20$. The diagrams show between $t_0 - 10$ and $t_0 + 10$ the westward propagation of positive values of relative vorticity at 17.5°N , at an approximate mean phase speed of 4° longitude per day, concomitant with the enhancement of dry convection in the heat low at the same latitude and with a decrease of the 400-hPa upward velocity at 10°N . These signals are maintained mainly during the phase of decreasing then increasing rainfall at 10°N characterizing the specific summer monsoon onset over West Africa.

Figure 11a shows the composite unfiltered NCEP–NCAR 925-hPa wind field at $t_0 - 15$. Colored areas depict relative vorticity values and the solid line is the zero isoline of the zonal wind component depicting the

ITF over the Sahel. The different positive maxima of vorticity along the ITF localize the semipermanent cyclonic vorticity centers. Four maxima are identified over land at 30° , 15°E , 0° , and 15°W . Fifteen days after, at t_0 (Fig. 11b), the ITF has moved a bit northward. Figure 11d shows the composite wind field of the difference between t_0 and $t_0 - 15$. Colored areas depict OLR differences and isolines relative vorticity differences. The northward ITF location at t_0 is depicted in Fig. 11d by positive relative vorticity anomalies between 15° and 25°N and southwesterly wind anomalies on the southern side. However, the positive anomalies of vorticity are greater east of 0° . Associated with this vorticity field, negative OLR anomalies, meaning greater convection, are located mostly east of 5°E . They are located along 12.5°N , on the northern boundary of the ITCZ still located at 5°N . Small negative OLR anomalies also occur over the ocean north of the ITCZ. Positive OLR anomalies along 2.5°N sign the northward progression of the ITCZ southern boundary. Between approximately 10°W and 5°E , only positive OLR anomalies are observable, signaling the convection decrease at these longitudes just before the monsoon onset (Fig. 6).

Figure 11e shows the difference fields between $t_0 - 10$ and $t_0 + 10$. The OLR pattern is similar to the previous one but amplified. However, the relative vorticity field is different. The greatest anomalies are now located on the western part of northern Africa, and especially west of 5°E . This leads to developed southwesterly anomaly winds over West Africa and over the northern tropical Atlantic. At the same time, we can observe an amplification of an anticyclonic circulation along 30°N north of the Atlas Mountains (see Fig. 12), and of as-

Figure 14b shows the composite time series from $t_0 - 90$ to $t_0 + 140$ of the 925-hPa geopotential height difference between values at 30°N , 7.5°E (point labeled 2 in Fig. 14a) and 22.5°N , 10°W (point 1; thick curve), of the 925-hPa geopotential height difference between values at 30°N , 7.5°E (point 2) and 17.5°N , 15°E (point 3; thin curve), and of the averaged 10°W – 10°E 600-hPa vertical velocity at 27.5°N (dashed curve). The thick and the thin curves again highlight the abrupt change of the atmospheric circulation with their steep slope occurring from $t_0 - 10$ to $t_0 + 20$, following a rather stable state before $t_0 - 10$. The time series of the geopotential heights associated to the anticyclonic center and to the cyclonic centers separately show an abrupt break around $t_0 - 10$ (not shown). The dashed curve in Fig. 14b shows the downward vertical velocity at 27.5°N , that is the location of both the northern subsiding branch of the heat low and the northern Hadley-type cell (Fig. 8). The subsidence in this area begins to increase around $t_0 - 35$, then more rapidly from $t_0 - 20$ to $t_0 + 40$. This enhancement is due first to the northern extension of the subsiding part of the transverse cell associated to the heat low and to its intensification around t_0 , second to the large development of the northern Hadley-type cell after t_0 , in particular of its northern subsiding part. So the windward subsidence and high geopotentials begin to increase first, increasing then the associated northeasterly winds, leading finally to the leeward cyclonic circulation enhancement.

Figure 14c shows the latitude–time cross section of the 600-hPa geopotential heights averaged over 10°W – 10°E . Figure 7f has highlighted the meridional abrupt shift of the zonal winds at 600 hPa between 20° and 30°N signing a similar shift of the axis of the high geopotentials at this pressure level. We see in Fig. 14c that it is concomitant with a strong increase of the geopotential heights to the highest values reached during the summer. This anticyclonic center is located after the monsoon onset above and northward of the North Africa highlands, and it is associated with the enhancement of the subsiding motions of the northern Hadley-type circulation. This signal of the monsoon onset can be put in parallel with the Asian monsoon onset where a similar northward abrupt shift of the subtropical westerly jet and the associated subtropical high pressures have been identified in the high troposphere above the Tibet highlands (Hahn and Manabe 1975).

Figure 14a shows a background signal specific to the West African summer monsoon onset over the period 1968–90. We have investigated the interannual variability associated with this pattern by performing an automatic classification (Janicot 1992) of these geopotential fields (not shown). We obtained four classes with similar spatial patterns, retaining the three centers (labeled 1, 2, and 3 in Fig. 14a) at about the same locations, with similar geopotential height gradient signs, but with different height amplitudes associated with these centers. However we could not define any

significant characterization of the ITCZ shifts related to these different classes (the four averaged rainfall fields depict a similar abrupt shift), nor any correlation with the summer rainfall amount over the Sahel. This suggests 1) the independency between the mechanisms associated to the interannual rainfall variability of the West African monsoon and the mechanisms induced in the monsoon onset, and 2) the hypothesis that the orography-induced mechanisms shown by Semazzi and Sun on the mean strength of the West African monsoon can work in the monsoon onset of individual years.

We suggest that the northern progression of the heat low and its transverse circulation leads to the enhancement of the anticyclonic circulation on the windward side of the Atlas–Ahaggar Mountain crest, inducing enhanced northeasterly winds that interact with the orography and lead to the increase of the leeward trough and associated westerly advection of moisture inland, contributing to the enhancement of the heat low intensity at t_0 . Then the ITCZ moves to the north and intensifies after breaking the convective inhibition induced by the heat low. This leads to the enhancement of the northern Hadley-type cell and to the development of its northern subsiding branch, which also contributes to increase the high geopotentials north of the mountains and then the orography-induced lee-trough southward. The abrupt shift of the ITCZ could then be explained by a positive feedback between the atmospheric circulation of the heat low, the convection in the ITCZ, and the Hadley-type circulation, through the control by the orography. The apparent westward signal seen in the filtered wind fields could be due to the northwest–southeast orientation of the orography axis, which induces the interaction with the heat low first in the east where the mountains are nearer to the ITF than in the west, and second in the west. The fact that we observe an abrupt shift of the ITCZ only in the western part of West Africa might result from the enhancement of moisture advection that comes from the west and has a stronger impact west of the Greenwich meridian.

6. Synthesis and conclusions

As the seasonal cycle advances in the first half of the year, a land–sea temperature gradient grows between West Africa and the equatorial and southern Atlantic basin, and the resulting low-level meridional pressure gradient moves northward. Over West Africa, the high northward temperature gradient and the high southward moisture gradient between the Sahara and the Guinean coast induce a meridional lag between the surface dry static energy maximum (located more northward) and the moist static energy (located more southward). This shows that the deep convection in the ITCZ controlling the two Hadley-type cells is located to the south of the dry convection of the heat low, limited in the low and midlevels of the troposphere, and capped by the subsiding branch of the northern Hadley-type cell. The

ground location of the heat low is also characterized by a positive relative vorticity maximum and by the confluence of the moist southwesterly winds of the monsoon and the dry northeasterly Harmattan, that is the ITF. At the preonset of the summer monsoon, that is at approximately $t_0 - 40$ days (where t_0 means the date of the summer monsoon onset), the ITF is located at 15°N and the ITCZ at 5°N . Between $t_0 - 40$ and $t_0 - 10$, the heat low dynamics dominates north of the ITCZ and a part of its northern subsiding area is located above and north of the Atlas–Ahaggar crest. During that time, isolated convective systems begins to occur south of the ITF, contributing to the northern progression of the ITCZ northern boundary, and may be to a slight increase of the northern Hadley-type cell dynamics and its subsiding motions, reinforcing the subsidence over the Atlas–Ahaggar orography. These two factors contribute to enhance the high geopotentials north of these mountains and the associated northeasterly winds.

Between $t_0 - 10$ and t_0 , the interaction between orography and northeasterly winds on the windward side of these mountains enhances and lead to the development of a leeward trough that reinforces the heat low dynamics. This has opposite consequences. On one hand, the midlevel subsidence of the southern branch of the heat low transverse circulation increases and may be accompanied by intrusion of dry air from the north. This can increase convective inhibition in the ITCZ and explain the observed temporary convection and rainfall decrease. On the other hand, cyclonic vorticity increases at low levels contributing to a greater inland moisture advection by stronger southwesterly winds and a deeper monsoon layer. In the midlevels, the anticyclonic circulation increases leading to the enhancement of the AEJ. Then the vertical wind shear between the low and midlevels becomes higher. Deeper monsoon and higher vertical wind shear enhance the local potential instability. The observed weaker convection also leads to higher downward solar radiation received at the surface (seen in the NCEP reanalysis; not shown), a favorable condition for potential instability increase. Finally as the heat low transverse circulation also maintains the instability of the AEJ by imposing a reversal of the meridional gradient of potential vorticity (Thorncroft and Blackburn 1997), the enhanced heat low dynamics increases the instability character of the AEJ (negative meridional gradient of potential vorticity is enhanced at 10°N between $t_0 - 10$ and t_0 ; not shown), which may favor easterly wave development and then convection.

From t_0 to $t_0 + 20$, the accumulated potential instability breaks the convective inhibition, the inertial instability of the monsoon circulation is released and the associated regional scale circulation increases, leading to the abrupt shift of the ITCZ. Then the ITCZ moves to the north, where thermodynamical conditions are favorable, up to 10°N . The northern Hadley-type circulation drastically enhances, which leads to the development of subsidence in the whole troposphere between

25° and 30°N . Then geopotential highs increases north and above the Atlas–Ahaggar Mountains, which enhances the orography-induced windward high and leeward trough again, maintaining an active convective ITCZ during the summer monsoon. The abrupt shift of the ITCZ could then be explained by a positive feedback between the atmospheric circulation of the heat low, the convection in the ITCZ, and the northern Hadley-type circulation, through an interaction with the orography.

The northwest–southeast orientation of the Atlas–Ahaggar crest can induce the interaction with the heat low first in the east where the mountains are nearer to the ITF than in the west, and second in the west. The fact that we observe an abrupt shift of the ITCZ only in the western part of West Africa may result from the enhancement of moisture advection that comes from the west and has a stronger impact west of the Greenwich meridian.

Another consequence of the orography-induced interaction with the atmospheric circulation is that the induced leeward trough, increasing the cyclonic vorticity in the heat low, may stimulate moisture convergence in the oceanic ITCZ near the western coast of West Africa. However, a similar ITCZ abrupt shift is not observed over this part of the northern tropical Atlantic.

Finally, once the monsoon onset occurs, the developed northern Hadley-type circulation can favor intrusion of dry air from the north and the upper levels into the ITCZ. These intrusions can be also controlled by the northerly winds of the heat low transverse circulation. This question has been addressed in Sultan et al. (2003) through the study of the intraseasonal timescale modulation of convection observed during the West African summer monsoon. This mechanism should not work efficiently before the summer monsoon onset since at this time the northern Hadley-type cell is not developed enough to the north to allow northerly advections far from the ITCZ.

The hypothesis of the abrupt shift of the ITCZ has been deduced from the observations. It must be confirmed through other ways of investigation. In particular atmospheric GCM experiments similar to that of Semazzi and Sun, but in the context of the seasonal cycle, would be a good way to test this hypothesis. However, these types of models have to first accurately reproduce the dynamics of the West African monsoon described here to be validated (Vernekar and Ji 1999). On the other hand, the hypothesis presented here is not necessarily the only explanation for the ITCZ abrupt shift. For instance, interactions between land surface processes and deep convection, especially through the impact of soil moisture and of the sensible heat input in the boundary layer, have been previously involved to explain northward-propagating rain bands in the Indian monsoon (Webster 1983; Gueremy 1990; Ferranti et al. 1999). Similar mechanisms could be involved in the ITCZ latitudinal shift over West Africa. Xie and Saiki (1999)

have proposed another mechanism to explain delayed abrupt onsets observed in the Asian summer monsoons by the concept of “geostrophic monsoon”: in a rotating atmosphere, the land–sea temperature difference does not necessarily lead to a direct overturning cell, but instead can be balanced by adjusting its vertical shear so as to be in a thermal wind balance with the meridional temperature gradient; so the onset is delayed and can be initiated by the explosive growth of a traveling disturbance. Plumb and Hou (1992) also showed that such a thermal wind adjustment is possible for an off-equatorial heating, and that an intensive meridional circulation occurs when the subtropical heating rate exceeds a certain threshold, another source for an abrupt change of the monsoon circulation and its onset. These types of mechanisms must be investigated further through ocean–atmosphere coupled GCMs since the monsoon onset could have a significant impact on the oceanic ITCZ near the western coast of West Africa.

In this work, by using gridded rainfall and NCEP–NCAR reanalysis data during the period 1968–90 (OLR was used since 1979), we have described the arrival of the summer monsoon over West Africa and characterized two steps: its preonset and its onset. We have shown that these steps are not correlated in time nor correlated with the summer rainfall amount over the Sahel. The results on the definition of these steps have been obtained through the computation of composite means based on the preonset or the onset date for each year. This method assumes that the rate of development before and after each of these steps is similar each year. We have characterized the preonset stage of the summer monsoon by the arrival of the ITF at 15°N around mid-May while the ITCZ is still centered at 5°N. The onset has been pointed out by an abrupt latitudinal shift of the ITCZ in late June from 5° to 10°N. This composite approach enables to highlight the atmospheric processes associated with these steps of the West African monsoon seasonal cycle. It could be thought that the composite procedure introduces artificial signals since, for the monsoon onset for instance, as we select t_0 so as to detect a shift, it is logical to find such a shift. However Le Barbé et al (2002) found a similar meridional shift of the ITCZ by computing a classic average of the rainfall seasonal cycle. So our composite approach, not only does not create the ITCZ shift, but enables us to focus more precisely on the associated dynamical mechanisms.

This is not only an interesting meteorological and climatological issue, it is also a major point for agriculturists. A better knowledge of the mechanisms of the arrival of the summer monsoon should help providing efficient forecast of the beginning of the growing season. This point has not been considered here since we have used a smoothing procedure to remove high-frequency transient signals from the composite rainfall and dynamical patterns associated to the summer monsoon onset. Forecasting this onset in an operational context need

to take these transients into account, in addition to the composite scenario proposed here.

Acknowledgments. We are thankful to the NOAA–CIRES Climate Diagnostics Center (Boulder, CO) for providing the NCEP–NCAR reanalysis dataset and the interpolated OLR dataset from their Web site (<http://www.cdc.noaa.gov/>). We also thank the two reviewers for their help improving this paper. This research was in part supported by the EC Environment and Climate Research Programme (Contract: EVK2-CT-1999-00022).

REFERENCES

- Ati, O. F., C. J. Stigter, and E. O. Oladipo, 2002: A comparison of methods to determine the onset of the growing season in northern Nigeria. *Int. J. Climatol.*, **22**, 731–742.
- Diedhiou, A., S. Janicot, A. Viltard, P. de Felice, and H. Laurent, 1999: Easterly wave regimes and associated convection over West Africa and the tropical Atlantic: Results from NCEP/NCAR and ECMWF reanalyses. *Climate Dyn.*, **15**, 795–822.
- Duvel, J. P., 1989: Convection over tropical Africa and the Atlantic Ocean during northern summer. Part I: Interannual and diurnal variations. *Mon. Wea. Rev.*, **117**, 2782–2799.
- Ferranti, L., J. M. Slingo, T. N. Palmer, and B. J. Hoskins, 1999: The effect of land-surface feedbacks on the monsoon circulation. *Quart. J. Roy. Meteor. Soc.*, **125**, 1527–1550.
- Gibson, J. K., P. Kalberg, S. Uppala, A. Hernandez, A. Nomura, and E. Serrano, 1997: ERA description. ECMWF Re-Analysis Project, Rep. Series 1, ECMWF, Reading, United Kingdom, 72 pp.
- Gruber, A., and A. F. Krueger, 1984: The status of the NOAA outgoing longwave radiation data set. *Bull. Amer. Meteor. Soc.*, **65**, 958–962.
- Gueremy, J. F., 1990: Heat and moisture fluxes on the time scale of 20 to 60 days over the Indian monsoon area. *Meteor. Atmos. Phys.*, **44**, 219–250.
- Hahn, D. G., and S. Manabe, 1975: The role of mountains in the South Asian monsoon circulation. *J. Atmos. Sci.*, **32**, 1515–1541.
- Hastenrath, S., 1995: *Climate Dynamics of the Tropics*. Kluwer, 488 pp.
- Janicot, S., 1992: Spatiotemporal variability of West African rainfall. Part I: Regionalizations and typings. *J. Climate*, **5**, 489–497.
- , S. Trzaska, and I. Pocard, 2001: Summer Sahel-ENSO teleconnection and decadal time scale SST variations. *Climate Dyn.*, **18**, 303–320.
- Kalnay, E., and Coauthors, 1996: The NCEP/NCAR 40-Year Reanalysis Project. *Bull. Amer. Meteor. Soc.*, **77**, 437–471.
- Kanamitsu, M., W. Ebisuzaki, J. Woollen, S.-K. Yang, J. J. Hnilo, M. Fiorino, and G. L. Potter, 2002: NCEP-DOE AMIP-II reanalysis (R-2). *Bull. Amer. Meteor. Soc.*, **83**, 1631–1643.
- Lamb, P. J., 1983: West African water vapor variations between recent contrasting Saharan rainy seasons. *Tellus*, **35A**, 198–212.
- Le Barbé, L., T. Lebel, and D. Tapsoba, 2002: Rainfall variability in West Africa during the years 1950–90. *J. Climate*, **15**, 187–202.
- Liebmann, B., and C. A. Smith, 1996: Description of a complete (interpolated) outgoing longwave radiation dataset. *Bull. Amer. Meteor. Soc.*, **77**, 1275–1277.
- Plumb, R. A., and A. Y. Hou, 1992: The response of a zonally symmetric atmosphere to subtropical thermal forcing: Threshold behavior. *J. Atmos. Sci.*, **49**, 1790–1799.
- Pocard, I., S. Janicot, and P. Camberlin, 2000: Comparison of rainfall structures between NCEP/NCAR reanalysis and observed data over tropical Africa. *Climate Dyn.*, **16**, 897–915.
- Richman, M. B., 1986: Rotation on principal components. *J. Climatol.*, **6**, 293–335.

- Semazzi, F. H. M., and L. Sun, 1997: The role of orography in determining the Sahelian climate. *Int. J. Climatol.*, **17**, 581–596.
- Sow, C. S., 1997: Diurnal rainfall variations in Senegal. *Secheresse*, **8**, 157–162.
- Sultan, B., 2002: Study of the monsoon onset in West Africa and of the convection intraseasonal convection. Application to the crop yield sensitivity (in French). Ph.D. thesis, 283 pp.
- , and S. Janicot, 2000: Abrupt shift of the ITCZ over West Africa and intra-seasonal variability. *Geophys. Res. Lett.*, **27**, 3353–3356.
- , ———, and A. Diedhiou, 2003: West African monsoon dynamics. Part I: Documentation of intraseasonal variability. *J. Climate*, **16**, 3389–3406.
- Thorncroft, C. D., and M. Blackburn, 1997: On the maintenance of the African Easterly Jet. *Quart. J. Roy. Meteor. Soc.*, **123**, 763–786.
- Tomas, R. A., and P. J. Webster, 1997: The role of inertial instability in determining the location and strength of the near-equatorial convection. *Quart. J. Roy. Meteor. Soc.*, **123**, 1445–1482.
- Vernekar, A. D., and Y. Ji, 1999: Simulation of the onset and intraseasonal variability of two contrasting summer monsoons. *J. Climate*, **12**, 1707–1725.
- Viltard, A., H. Laurent, and P. de Felice, 1990: Lower-tropospheric cyclonic vorticities in northern Africa in summer. *Mon. Wea. Rev.*, **118**, 818–823.
- Webster, P. J., 1983: Mechanisms of monsoon low-frequency variability: Surface hydrological effects. *J. Atmos. Sci.*, **40**, 2110–2124.
- Xie, S. P., and N. Saiki, 1999: Abrupt onset and slow seasonal evolution of summer monsoon idealized GCM simulation. *J. Meteor. Soc. Japan*, **77**, 949–968.